Wide-Band Vertical Superconducting Accelerometer for Simultaneous Observations of Temporal Gravity and Ambient Seismic Noise

Dong Ma, Xikai Liu, Mao Zhang, Ning Zhang,[†] Liang Chen, and Xiangdong Liu[*]
MOE Key Laboratory of Fundamental Physical Quantities Measurement & Hubei Key Laboratory of Gravitation and Quantum Physics, PGMF and School of Physics, Huazhong University of Science and Technology, Wuhan 430074, P. R. China

(Received 7 May 2019; revised manuscript received 29 August 2019; published 22 October 2019)

Ambient seismic noise contains valuable information about the structural properties of Earth's subsurface. The superconducting gravimeter (SG) is the most suitable instrument for temporal gravity, but not for microseisms due to its limited bandwidth. We report an alternative type of vertical superconducting accelerometer with a bandwidth as high as 0.7 Hz. Its sensitivity is comparable with the current SG. The accelerometer consists of a superconducting mass-spring oscillator and a displacement sensor based on a superconducting quantum interference device. The oscillator is constructed by levitating a Meisnner-state proof mass using combined positive-stiffness and negative-stiffness superconducting coils. Its natural frequency can be adjusted by the coil currents over a large range. The enhanced sensitivity of displacement sensing compensates the sensitivity loss imposed by the broadened bandwidth. Experimental tests show that both the gravity variation and the microseism can be extracted from the measurement data. It would be quite meaningful to monitor the temporal gravity and structural evolution using such an accelerometer array in sensitive zones, for example, the crustal fault and volcano zones.

DOI: 10.1103/PhysRevApplied.12.044050

I. INTRODUCTION

The superconducting gravimeter (SG) [1] has been one of the most important instruments for observations of temporal gravity since its invention [2]. The perfect stability of the superconducting levitation makes it an unmatched instrument for gravity observations at periods from minutes to years. The successful application of SGs has enabled an unprecedented series of tests and improved understanding of geodynamic problems, such as atmospheric loading, ocean loading, tectonic motion, and Earth's rotation and polarmotion [3].

The vertical superconducting accelerometer is the core unit for SGs. In the GWR Instruments Inc. (GWR) SGs, the accelerometer is constructed with a spring oscillator based on a superconductively levitated proof mass and a capacitive displacement sensor. To achieve a large enough transfer factor of displacement upon acceleration, the superconducting oscillator is elaborately designed to have a low natural frequency, which is less than 0.25 Hz [4]. In addition, heavy damping is applied to reduce the resonant displacement response, thus making room to increase the gain of the displacement detection. This design strategy guarantees a high sensitivity for low-frequency gravity signal measurements required for SGs. Furthermore, the low natural frequency helps to suppress the motion response of the oscillator to high-frequency seismic signals, which is considered as useless noise for gravity observations. Consequently, the seismic perturbation is minimized. Viewed in every aspect, the GWR SG sets a near-perfect example for gravity instrumentation.

Today, the situation has changed a little. As an important breakthrough, an alternative approach to geophysical observation called ambient noise cross-correlation has been well established in the past two decades [5,6]. In this approach, valuable structural information about Earth's crust and upper mantle can be extracted from multisite data of ambient seismic noise by correlation analysis. Thus, the ambient noise acts as a persistent illuminator for structural imaging [7]. For this purpose, the seismic noise within the frequency band from 0.01 to 1 Hz is most frequently chosen due to the high signal-to-noise ratio. The GWR SGs can see it, but the frequency-dependent transfer factor of the oscillator and the heavy damping-induced phase delay prevent a precise measurement [8]. One would wonder whether the SG's frequency band can be broadened to cover the ambient noise without loss of its sensitivity. If so, both the gravity variation and velocity structure evolution can be observed with several SGs. This is especially meaningful for the geodynamic monitoring of sensitive zones [9], such as crustal fault zones [10], volcano zones [11], and those covered with ice sheets [12].

[*]liuxd@mail.hust.edu.cn
[†]ningzhang@hust.edu.cn

Keeping the above in mind, we develop an alternative type of vertical superconducting accelerometer (VSA). The natural frequency f_0 of the superconducting oscillator is designed to be 2.7 Hz and the quality factor Q is about 30. The high f_0 and large Q allow the oscillator's transfer function to remain flat up to at least 0.7 Hz. The noise floor of the accelerometer is estimated to be lower than 2×10^{-9} m/s^2/$\sqrt{\text{Hz}}$ from 1×10^{-5} to 1 Hz, enough to meet the sensitivity requirements for various applications. Experimental tests show that the low-frequency tide signal and the high-frequency microseism can be simultaneously monitored with high sensitivity by our superconducting accelerometer.

II. DESIGN AND WORKING PRINCIPLE

A. Structure and circuit

As a general concept, the accelerometer consists of a superconducting mass-spring oscillator, which transduces acceleration to displacement followed by a displacement sensor. In the context of the mass-spring model, high sensitivity and wide bandwidth are always contradicted. High sensitivity requires a low natural frequency to obtain a large transfer function from acceleration to displacement, whereas the low natural frequency limits the bandwidth. Such a transfer function remains flat only below the natural frequency. In order to sustain a high sensitivity in a wide bandwidth, three tricks are used in the design of the current VSA.

First, the displacement detection unit is constructed with a dc superconducting quantum interference device (SQUID) based on superconducting circuits that Chan and Paik pioneered in their gravity gradiometers [13–15]. The perfect combination of the noiseless superconducting circuit and the low-noise current-to-voltage amplifier (SQUID) makes it one of the most sensitive methods for sensing tiny displacements [16–19]. The introduction of SQUIDs for displacement sensing compensates the sensitivity loss due to the broadening of the frequency band. Second, strong constraints are imposed to the motion of the proof mass in the nonsensitive degrees of freedom (DOF), so that the cross-coupling effects are sufficiently suppressed when the broadened band covers the seismic microseism. This is realized by setting the oscillator stiffness at the nonsensitive DOF larger than that of the vertical one by at least two orders of magnitude. Third, a resistive damping mechanism based on a superconducting circuit is introduced to the oscillator, which allows the quality factor Q to be set to the optimized value by the circuitry. The Q factor is designed to fall in the range from 10 to 50. This parametric choice may keep the amplitude-frequency and phase-frequency response curves flat up to a high frequency while the resonant response of the displacement is still acceptable.

The basic structure of the VSA is illustrated in Fig. 1(a). The 100-gram-niobium proof mass takes the shape of a cylinder with a middle blinding plate, following the ARKeX superconducting gravity gradiometer [18]. In the cylinder, two superconducting pancake coils are mounted coaxially with the proof mass, with one under the blinding plate and the other over it. In addition to the pancake coils, a superconducting solenoid coil is also mounted coaxially with the proof mass. The outer diameter of the solenoid is smaller than the inner diameter of the proof mass by 1–2 mm. The solenoid is located near the bottom edge of the proof mass with part of it inside the cylinder. These three coils allow the sensitive DOF to levitate the proof mass and to detect its vertical motion. Benefitting from the cylindrical symmetry of the proof mass, eight

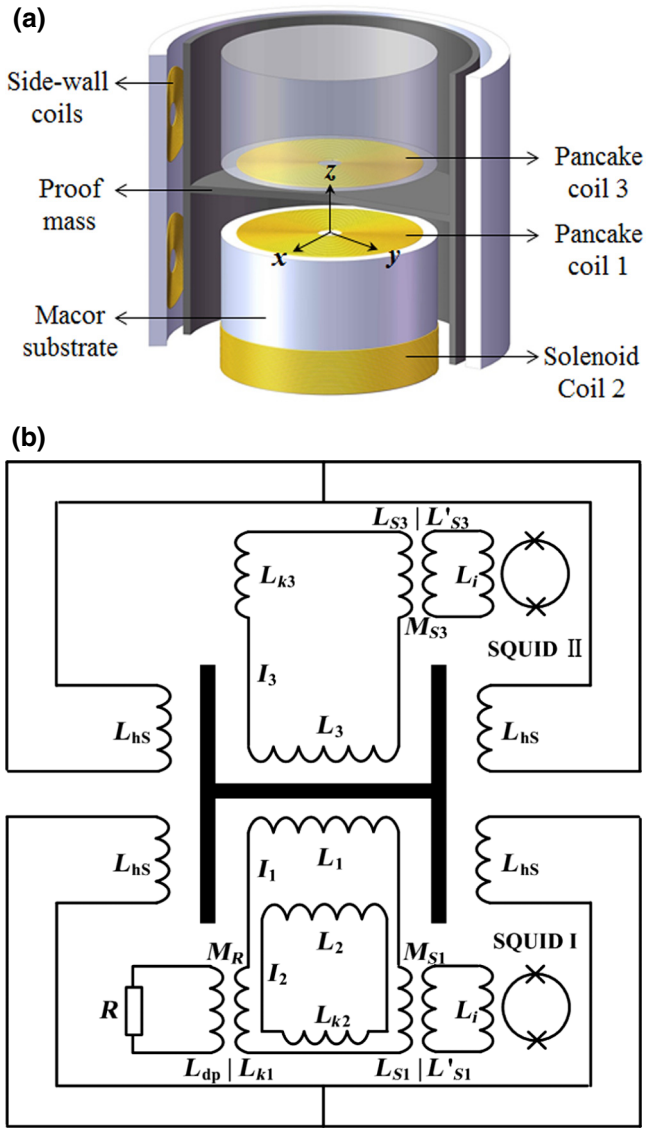

FIG. 1. (a) Illustration of the VSA structure. (b) The superconducting circuits for the VSA.

TABLE I. VSA design parameters.

Component	Dimensions (mm)	Position (mm)
Proof mass	$D50 \times H50 \times t1.25$[a]	$z = +0.75$[b]
Pancake coil 1	$d6 \times D36.8 \times N110$[c]	$z = 0$[d]
Solenoid coil 2	$d44.5 \times D45.7 \times L8$[e] $\times N200$	$z = -19.37$[f]
Pancake coil 3	$d6 \times D36.8 \times N110$	$z = +2.75$
Side-wall coils	$d6 \times D18.6 \times N45$	$\Delta r = 0.5$[g]

[a] D, H, and t, respectively, represent the outer diameter, height, and thickness.
[b] $+0.75$ means the upward spacing relative to the pancake coil 1.
[c] d, D, and N, respectively, represent the inner diameter, outer diameter, and number of turns.
[d] The coordinate system locates at the center of pancake coil 1.
[e] L represents the length.
[f] -19.37 means the downward spacing relative to the pancake coil 1.
[g] Δr represents the radial spacing with the proof mass's external wall.

superconducting coils with the same designed electromagnetic and geometrical parameters can be mounted around the lateral wall of the cylinder. These side-wall coils interact with the proof mass and provide a large stiffness for the nonsensitive DOF except for the vertical rotation. With the sensitive coils placed inside the cylinder and the nonsensitive ones outside, the proof mass can efficiently separate the magnetic fields from each other due to the Meissner effect. Thus, the cross-coupling effects can be minimized. The design parameters are given in Table I.

The superconducting circuits are given in Fig. 1(b). As aforementioned, there are three superconducting coils directly interacting with the proof mass for the sensitive DOF, that is, the lower pancake coil L_1, the solenoid L_2, and the upper pancake coil L_3. Associated with these coils are three independent superconducting circuits. After persistent currents are injected into the loops, L_1 and L_2 exert an upward vertical force on the proof mass and jointly levitate the proof mass. Though the force exerted by L_3 is downward, the introduction of L_2 is quite helpful for obtaining a flat and symmetric stiffness curve with respect to the vertical displacement of the proof mass at its equilibrium position. In each loop, a large-inductance superconducting coil is incorporated to adjust the stiffness. They are denoted as L_{k1}, L_{k2}, and L_{k3}, respectively. These coils do not interact with the proof mass and their inductances remain constant (Table II). Their function is to attenuate the variation of the loop current resulting from the motion of the proof mass, and thus lower the oscillator stiffness to a suitable value.

Coils L_1 and L_3 work as pick-up coils for the displacement detection as well. Their inductances change linearly with the vertical displacement of the proof mass at the first-order approximation. Governed by the flux conservation law of superconducting loops, the loop current then changes spontaneously with the variation of inductance. Via superconducting transformers (M_{S1} and M_{S3}), the variable current is measured by SQUIDs with high resolution. The sensitivity of the displacement detection can be tuned by the parameters of the transformer. The sensitivity of the L_3 loop is designed to be smaller than that of the L_1 loop by one order of magnitude in order to guarantee that large-amplitude earthquake signals can be safely recorded.

TABLE II. Estimated inductance value (proof mass at $z = +0.75$ mm).

	Coils					
Parameter	L_1	L_2	L_3	L_{k1}	L_{k2}	L_{k3}
Inductance (μH)	42.1	872.9	42.1	3909.8	9275.5	5740.7

An additional loop consisting of a superconducting coil $L_{\rm dp}$ and a resistor R is constructed to provide the necessary damping for the vertical oscillator. Letting coil $L_{\rm dp}$ be coupled with L_{k1}, voltage will be applied across the dissipative resistor when the persistent current in the L_1 loop varies. The damping strength can be adjusted by the resistance and the coupling coefficient between $L_{\rm dp}$ and L_{k1}.

For the side-wall coils, the superconducting circuit is constituted by simply connecting its two leads using niobium wire. In this way, the maximized stiffness can be obtained for the nonsensitive DOF.

B. Levitation and stiffness adjustment

To calculate the natural frequency of the vertical oscillator, we first invoke the principle of flux conservation for the three loops of the sensitive DOF

$$[L_j(z) + L_{ej}]I_j(z) = \Phi_j \quad (j = 1, 2, 3), \tag{1}$$

where Φ_j is the initial trapped flux. $L_j(z)$ is the displacement-dependent inductance of the coils directly interacting with the proof mass. L_{ej} is the equivalent constant inductance, where $L_{e1} = L_{k1} + L_{S1} - M_{S1}^2/(L'_{S1} + L_i)$, $L_{e2} = L_{k2}$, and $L_{e3} = L_{k3} + L_{S3} - M_{S3}^2/(L'_{S3} + L_i)$. The mutual flux from the damping loop and that between L_1 and L_2 are estimated to be small enough to be ignored. To simplify the expression, these mutual inductances are assumed to be zero. The total stored energy can be expressed as

$$U = \frac{1}{2}\sum_{j=1}^{3}[L_j(z) + L_{ej}][I_j(z)]^2. \tag{2}$$

The restoring force and stiffness are given by

$$F = -\frac{\partial U}{\partial z} = \frac{1}{2}\sum_{j=1}^{3}\frac{\partial L_j(z)}{\partial z}[I_j(z)]^2, \tag{3}$$

$$k = -\frac{\partial F}{\partial z} = \sum_{j=1}^{3}\left\{\frac{1}{L_j(z)+L_{ej}}\left[\frac{\partial L_j(z)}{\partial z}\right]^2 - \frac{1}{2}\frac{\partial^2 L_j(z)}{\partial z^2}\right\}[I_j(z)]^2. \tag{4}$$

The natural frequency is given by $f_0 = \sqrt{k/m}/(2\pi)$, where m is the mass. Obviously, the stiffness depends on the first and the second derivatives of the coil inductance with respect to the displacement of the proof mass. The first term in Eq. (4) associated with the first derivative always contributes a positive stiffness, reflecting the effect of the variation of the loop current on the stiffness governed by the flux conservation law. The second term, in principle, can be positive or negative, depending on the configuration of the coil and the proof mass. For the pancake coil, the second derivative is negative, resulting in a positive contribution to the stiffness. Theoretical calculations show that the natural frequency cannot be smaller than 10 Hz if the proof mass is levitated by an individual pancake coil, no matter how the parameters are adjusted. This natural frequency is too high for high-resolution measurements. However, in some special configurations, such as the solenoid in the current work, the second derivative is positive, showing a negative contribution to the stiffness. Using the finite element method [20], we calculate the effective inductance at various proof mass positions and the results are plotted in Fig. 2(a). The curve is concave for the solenoid, indicating a positive second-order derivative. By incorporating a large superconducting inductor L_{k2} in the solenoid loop to reduce the positive component [refer to Eq. (4)], the stiffness contributed by the solenoid can be totally negative and its magnitude can be tuned by the loop currents.

The introduction of the solenoid not only lowers the oscillator stiffness but also enables the stiffness to be adjusted within a large range. Since the solenoid coil contributes to levitate the proof mass but presents a negative stiffness, one can properly distribute the loop currents to obtain the designed stiffness [21]. As shown in Fig. 2(b), three groups of combined current parameters are chosen to levitate the proof mass at the same position. The resultant oscillator natural frequencies are calculated to be 1.1, 2.8, and 4.0 Hz, respectively. In principle, the natural frequency can be set to an arbitrary value from 0^+ Hz to about 30 Hz if the current setting resolution is high enough.

C. Transfer function

The transfer function of the accelerometer can be factorized into two terms: the transfer function from acceleration to displacement depending on the oscillator's stiffness and its damping coefficient, and that from displacement to output voltage determined by the superconducting circuit and the SQUID device.

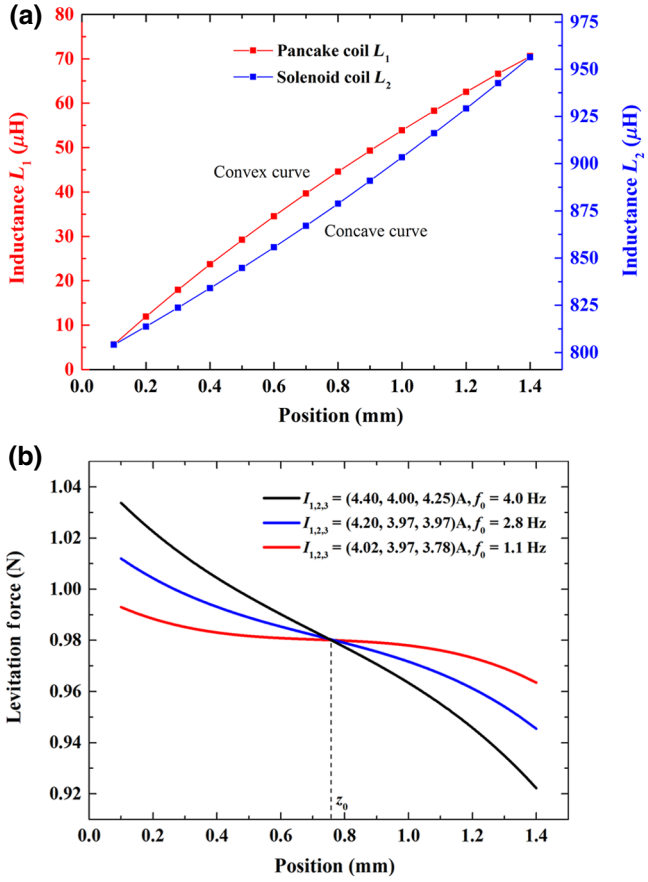

FIG. 2. (a) The effective inductances as a function of the proof mass position for the pancake coil and the solenoid, which are convex for the pancake coil and concave for the solenoid. (b) The magnetic levitation force as a function of the proof mass position. The stiffness is the slope of the curve at the equilibrium position ($z = +0.75$ mm). The current parameters in the figure correspond to the lower pancake coil, the solenoid, and the upper pancake coil, in that order.

In the current design, resistive damping is introduced into the superconducting circuit. The dynamic equation should include this effect. To do it, we first apply Kirchhoff's voltage equation to the damping loop, which yields

$$L_{\mathrm{dp}}\frac{di_R}{dt} + M_R\frac{dI_1(z)}{dt} + Ri_R = 0, \tag{5}$$

where i_R is the damping loop current. Let $\Delta i_j = I_j(z) - I_j(z_0)$, ($I_j(z_0)$ is the initial current), Laplace transform yields

$$i_R = -\frac{M_R}{R/s + L_{\mathrm{dp}}}\Delta i_1, \tag{6}$$

where s is the Laplace complex operator. The damping current i_R works by modulating the levitating current $I_1(z)$

via the superconducting transformer M_R. Now the dynamic equation can be written as

$$\frac{1}{2}\sum_{j=1}^{3}\frac{\partial L_j(z)}{\partial z}[I_j(z)]^2-\frac{1}{2}\sum_{j=1}^{3}\left.\frac{\partial L_j(z)}{\partial z}\right|_{z_0}[I_j(z_0)]^2 - c\Delta\dot{z}-m\Delta g=m\Delta\ddot{z}, \tag{7}$$

where c is the damping coefficient of residual gas and Δg is the gravity variation. Substituting Eq. (6) into Eq. (7) and using the Taylor linear approximation followed by Laplace transform again, one obtains

$$ms^2\Delta z+cs\Delta z + \sum_{j=1}^{3}\left\{\frac{1}{L_{aj}}\left[\left.\frac{\partial L_j(z)}{\partial z}\right|_{z_0}\right]^2-\frac{1}{2}\left.\frac{\partial^2 L_j(z)}{\partial z^2}\right|_{z_0}\right\} \times[I_j(z_0)]^2\Delta z=-m\Delta g, \tag{8}$$

where $L_{a1}=L_1(z_0)+L_{k1}+L_{S1}-M_{S1}^2/(L'_{S1}+L_i)-M_R^2/(R/s+L_{\rm dp})$, $L_{a2}=L_2(z_0)+L_{k2}$, and $L_{a3}=L_3(z_0)+L_{k3}+L_{S3}-M_{S3}^2/(L'_{S3}+L_i)$. The transfer function of the oscillator is deduced as

$$H_{gz}=\frac{\Delta z}{-\Delta g}=\frac{m}{ms^2+cs+k}, \tag{9}$$

where

$$k=\sum_{j=1}^{3}\left\{\frac{1}{L_{aj}}\left[\left.\frac{\partial L_j(z)}{\partial z}\right|_{z_0}\right]^2-\frac{1}{2}\left.\frac{\partial^2 L_j(z)}{\partial z^2}\right|_{z_0}\right\}[I_j(z_0)]^2,$$

represents the stiffness term.

Table III summarizes the design parameters. Substituting these values into Eq. (9), we calculate the amplitude and phase response functions in Fig. 3. The resonant frequency f_r is designed to be 2.7 Hz and the Q factor to be 30.9. Both functions remain flat at least up to 0.7 Hz. According to the principle of the accelerometer, the transfer function of the oscillator needs to remain flat near to 1 Hz in order to obtain a consistent scale factor.

Next, the transfer function from displacement to input current i_{S1} of the SQUID is given by two flux conservation equations

$$[L_1(z_0)+L_{e1}]I_1(z_0)=[L_1(z)+L_{e1}]I_1(z), \tag{10}$$

$$M_{S1}I_1(z_0)=M_{S1}I_1(z)+(L'_{S1}+L_i)i_{S1}. \tag{11}$$

Solving Eqs. (10) and (11) yields

$$H_{zi1}=\frac{i_{S1}}{\Delta z}=\left.\frac{\partial L_1(z)}{\partial z}\right|_{z_0}\frac{I_1(z_0)}{L_1(z_0)+L_{e1}}\frac{M_{S1}}{L'_{S1}+L_i}. \tag{12}$$

Thus, the final transfer function from displacement to output voltage is $H_{zv1}=H_{zi1}K_{iv}$, where $K_{iv}=1\times10^6$ V/A is the current-to-voltage amplifying coefficient of the SQUID. Obviously, this transfer function H_{zv1} is just a proportionality constant, which makes no difference to the system transfer function characteristic. A SQUID based displacement detector usually has a bandwidth of several tens of kilohertz. Therefore, the accelerometer's bandwidth is determined by the oscillator and it is also up to 0.7 Hz.

TABLE III. The relevant parameter values about the transfer function.

Damping of gas and resistor	
c (kg/s)	R (Ω)
0.015	0.017

Levitating currents (A)		
I_1	I_2	I_3
4.24	3.03	0.10

Inductance of transformers (μH)								
$L_{\rm dp}$	M_R	L_{S1}	L'_{S1}	M_{S1}	L_i	L_{S3}	L'_{S3}	M_{S3}
222.3	580.4	3.7	14.4	6.2	2.6	52.7	3.8	11.3

1st and 2nd derivatives of levitating coils inductance					
$\left.\frac{\partial L_j(z)}{\partial z}\right\|_{z_0}$ (H/m)			$\left.\frac{\partial^2 L_j(z)}{\partial z^2}\right\|_{z_0}$ (H/m^2)		
$j=1$	$j=2$	$j=3$	$j=1$	$j=2$	$j=3$
0.049	0.117	−0.049	−18.4	34.7	−18.4

D. Noise budget

The instrument noise of the VSA consists of three parts: the mechanical thermal noise, the resistor thermal noise, and the SQUID noise.

According to the fluctuation-dissipation theorem of Callen *et al.* [22,23], the power spectral density (PSD) of

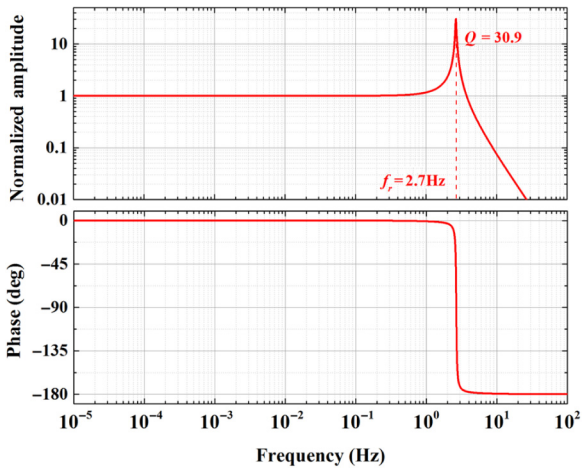

FIG. 3. The amplitude (upper panel) and phase (lower panel) response functions of the superconducting oscillator.

the displacement of the oscillator can be shown as [24]

$$\Delta z^2(\omega) = \frac{4k_B Tc}{(k - m\omega^2)^2 + (c\omega)^2}, \tag{13}$$

where k_B is the Boltzmann's constant, T is the operating temperature, and k is the stiffness of the oscillator. Consequently, the equivalent acceleration noise is

$$S_m = \frac{\Delta z^2(\omega)}{|H_{gz}|^2} = \frac{4k_B Tc}{m^2}. \tag{14}$$

The damping resistor also works as a noise source. On the basis of the fluctuation-dissipation theorem, the voltage PSD of R can be expressed as $V_R^2 = 4k_B TR$ [25]. Accompanying the voltage noise is the current noise in the levitating loop L_1. The noise current has two-fold effects. On one hand, it will disturb the motion of the proof mass as the levitating force varies with the levitating current, and the motion of the proof in turn modulates the current in the superconducting loops. On the other hand, it will be directly coupled into SQUID I. Taking these two effects into account, the equivalent acceleration PSD induced by the damping resistor is calculated as follows. Assuming that there is no input acceleration for the VSA, the input noise current of the SQUID i'_{S1} is obtained by solving Eqs. (15)–(18), which are the Kirchhoff voltage equation of the damping loop, the flux conservation equation of the levitating loops (L_1, L_2, L_3) and the sensing loop L'_{S1}, and the oscillator's dynamic equation, respectively,

$$V_R = L_{\rm dp}\frac{di'_R}{dt} + M_R\frac{di'_1}{dt} + Ri'_R, \tag{15}$$

$$[L_j(z_0) + L_{ej}]I_j(z_0) = [L_j(z) + L_{ej}][I_j(z_0) + i'_j] + \frac{(j-2)}{2(j-3)^{-1}}M_R i'_R \quad (j = 1,2,3), \tag{16}$$

$$M_{S1}I_1(z_0) = M_{S1}[I_1(z_0) + i'_1] + (L'_{S1} + L_i)i'_{S1}, \tag{17}$$

$$\frac{1}{2}\sum_{j=1}^{3}\frac{\partial L_j(z)}{\partial z}[I_j(z_0) + i'_j]^2 - \frac{1}{2}\sum_{j=1}^{3}\frac{\partial L_j(z)}{\partial z}\bigg|_{z_0}[I_j(z_0)]^2 - c\Delta\dot{z} = m\Delta\ddot{z}, \tag{18}$$

where i'_R and i'_j $(j = 1,2,3)$ represent the noise current in the damping and levitating loops, respectively. The result is

$$i'_{S1} = \frac{M_{S1}}{L'_{S1} + L_i}\left\{1 - [\frac{\partial L_1(z)}{\partial z}|_{z_0} I_1(z_0)]^2\frac{H_{gz}}{mL_{t1}}\right\} \frac{M_R V_R}{RL_{t1} + j\omega(L_{t1}L_{\rm dp} - M_R^2)}, \tag{19}$$

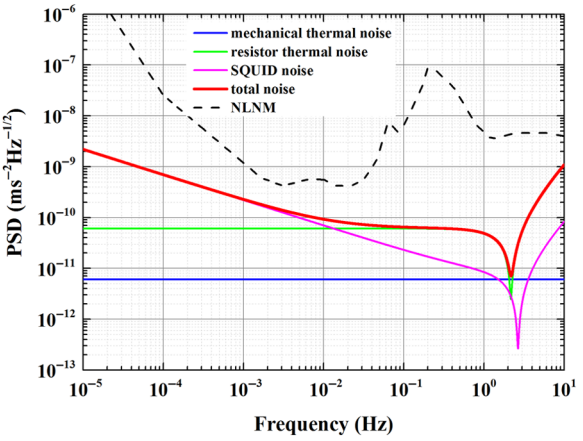

FIG. 4. The noise budget of the VSA.

where $L_{t1} = L_1(z_0) + L_{k1} + L_{S1} - M_{S1}^2/(L'_{S1} + L_i)$. By multiplying the reciprocal transfer function from the input acceleration to the SQUID input current, the equivalent acceleration PSD can be finally written as

$$S_R^{\rm I} = \left|\left[\frac{\partial L_1(z)}{\partial z}\bigg|_{z0}\frac{I_1(z_0)}{L_{t1}}H_{gz}\right]^{-1} - \frac{\partial L_1(z)}{\partial z}\bigg|_{z0}\frac{I_1(z_0)}{m}\right|^2 \frac{M_R^2 4k_B TR}{|RL_{t1} + j\omega(L_{t1}L_{\rm dp} - M_R^2)|^2}. \tag{20}$$

The SQUID noise has been modeled in terms of the energy sensitivity. It can be characterized as the sum of white and $1/f$ noise [26]. For a typical SQUID, it is

$$E_{\rm SQ} = (1 + 1\ {\rm Hz}/f) \times 3 \times 10^{-31}\ {\rm J/Hz}. \tag{21}$$

The energy sensitivity is related to the SQUID current noise by $E_{\rm SQ} = L_i i_S^2/2$, where L_i and i_S represent the input inductance and the current of the SQUID, respectively. Then this equivalent acceleration noise is

$$S_{\rm SQ}^{\rm I} = \frac{2E_{\rm SQ}}{L_i|H_{gz}H_{zi1}|^2}. \tag{22}$$

The noise budget of the accelerometer is shown in Fig. 4. In the frequency range from 0.01 to 1 Hz, the noise level is lower than 0.01 μGal/$\sqrt{\rm Hz}$. Below 0.01 Hz, it is dominated by the SQUID's $1/f$ noise, and reaches 0.2 μGal/$\sqrt{\rm Hz}$ at 1×10^{-5} Hz. In the full band, the accelerometer's noise is much lower than the new low-noise model (NLNM).

III. EXPERIMENTAL RESULTS

A superconducting accelerometer is fabricated following the above concepts and tested at 4.2 K. In the test setup, the accelerometer is suspended from the Dewar flange in

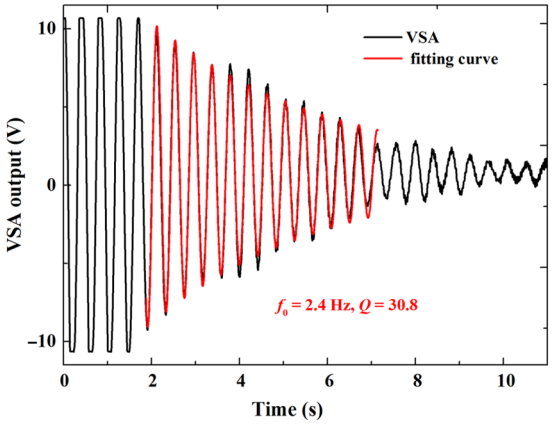

FIG. 5. The free oscillating trace of the proof mass after a transient excitation from which the resonant frequency and quality factor are measured.

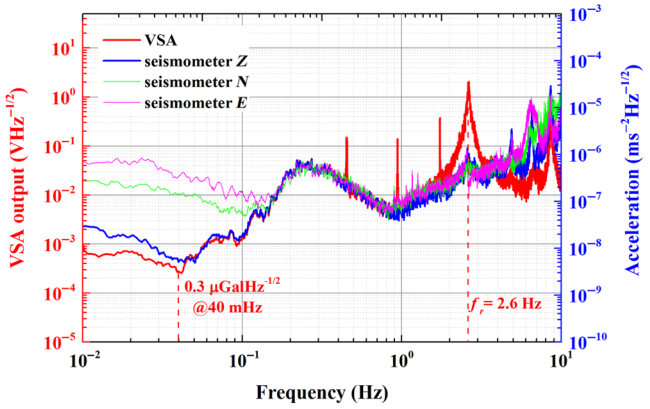

FIG. 6. The vertical seismic PSD measured by the VSA (red) compared with that by a CMG-3ESPC seismometer (blue). The horizontal seismic PSDs by the seismometer are also present.

vacuum by three stainless wires. The vacuum can is dipped in a liquid helium Dewar.

After applying a vertical transient excitation to the accelerometer, the time trace of the SQUID output monitoring the proof mass oscillation is recorded, as shown in Fig. 5. Fitting the data using the standard free oscillating model, the resonant frequency f_r and the quality factor Q are roughly determined to be 2.4–2.7 Hz and 30–31, respectively. It should be pointed out that the measured parameters vary by several percentages from one feeding procedure of the superconducting currents to another, despite the fact that the same current parameters are used. Most likely, the discrepancies reflect the different positions of the proof mass at the moment the heat switches are actually turned off. Since the effective inductance of the levitating coil depends on the position of the proof mass, the actual flux trapped in the loop also varies with the position. In the seismic environment, the latter is uncontrollable.

Lacking an effective method to measure the noise floor, we just set an upper limit for the superconducting accelerometer. This is done by operating it side by side with a calibrated CMG-3ESPC (120 SEC-50 Hz) seismometer. The PSD based on one hour data are shown in Fig. 6. Within the frequency range from 0.1 to 1 Hz, the PSD curves of the VSA output and the seismometer z axis data overlap well after setting a scale factor of 1410 μGal/V for the VSA, which is obtained by a least-square fitting of the data. Below 50 mHz, notable disparity appears. The VSA data shows a lower PSD than that of the seismometer and presents a minimum value of 0.3 μGal/$\sqrt{\text{Hz}}$ at 40 mHz. The low-frequency PSD measured by the VSA is lower than that of the horizontal seismic motion by about two orders of magnitude, implying a good suppression of the cross-coupling effects. Appearing on the VSA PSD curve, the broad peak around 2.6 Hz corresponds to the oscillator's resonance. The three sharp peaks originate from the suspension mechanism by which the VSA was installed in the Dewar.

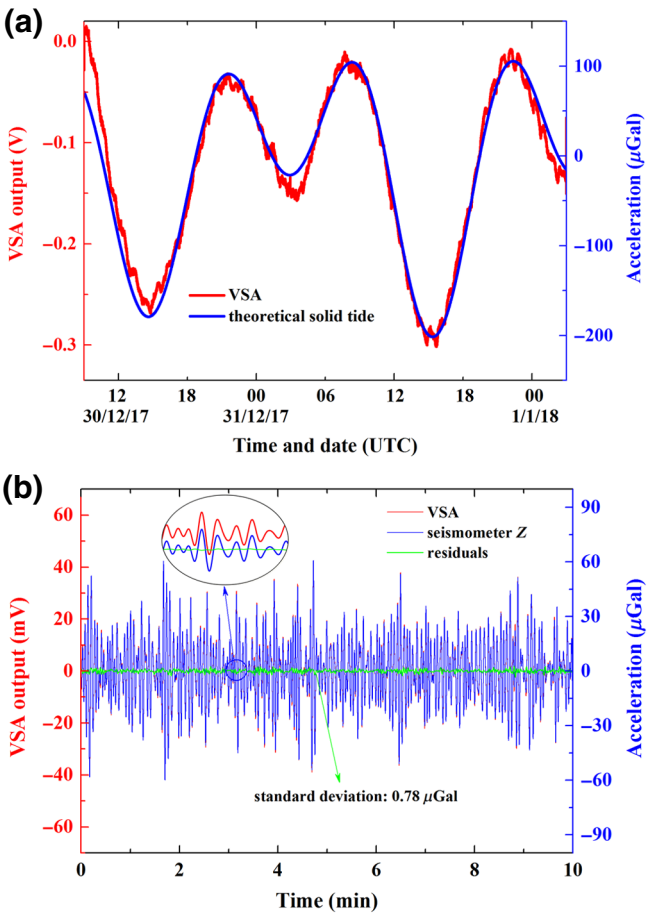

FIG. 7. (a) The measured Earth tides compared with the theoretical prediction. The theoretical solid tide is calculated with Tsoft. (b) The seismic microseism extracted from the tide data compared with that measured by a seismometer.

To check its stability, we try to monitor the Earth's tides with our VSA. Since the test was carried in a liquid helium Dewar without a cryocooler incorporated, the uninterrupted monitoring time was limited to 48 h. Figure 7(a) shows a typical result. The data record starts half an hour after the helium transfer. The data is recorded with a rate of 1000 samples per second and is processed by a simple slip averaging of 10 000 points (10 s). The measured tide curve deviates from the theoretical one in the early hours. This deviation diminishes with time. We attribute the deviation to the temperature drift induced by the liquid helium transfer. During the transfer, a 2 psi pressure is applied, elevating the temperature of the liquid helium Dewar from its equilibrium point by 0.14 K. When the temperature is stabilized, satisfactory agreement is observed between the measured and the theoretical tide. When the data processing method changes to a band-pass filtering from 0.05 to 0.4 Hz, the seismic microseism can be clearly seen, as shown in Fig. 7(b). The seismometer data in the same time segment is also present for a comparison. Linear regression is applied to give the residuals (the green line) between the VSA and the seismometer data, whose standard deviation is 0.78 μGal. The good agreement indicates that the VSA is capable of monitoring the Earth's ambient noise with high precision.

We conclude from the above results that the key performance parameters of the VSA comply with the design. Based on the VSA, a prototype of a superconducting gravimeter is under construction. A refrigeration system and the feedback control systems for temperature and tilt will be incorporated in it following the GWR gravimeter.

IV. CONCLUSION

We design and test a wide-band superconducting accelerometer. The accelerometer consists of one proof mass levitated spring oscillator and one SQUID based displacement sensor. The enhanced displacement sensitivity detection enables the superconducting oscillator to be designed with a high natural frequency so that the frequency band is broadened to cover the seismic microseism without loss of sensitivity. If such accelerometers are adopted to construct superconducting gravimeters, the temporal gravity and Earth's ambient noise can be measured simultaneously, thus extending the applications of the superconducting gravimeters to seismology.

ACKNOWLEDGMENTS

We thank Dr J-M Le Floch for revising our manuscript. This work is supported by the National Key R&D Program of China (Grants No. 2018YFC1503701 and No. 2017YFC0601605) and the National Natural Science Foundation of China (Grant No. 41474060).

[1] W. A. Prothero, and J. M. Goodkind, A Superconducting gravimeter. Rev. Sci. Instrum. **39**, 1257 (1968).
[2] J. M. Goodkind, The superconducting gravimeter, Rev. Sci. Instrum. **70**, 4131 (1999).
[3] J. Hinderer and D. Crossley, Scientific achievements from the first phase (1997–2003) of the global geodynamics project using a worldwide network of superconducting gravimeters, J. Geodyn. **38**, 237 (2004).
[4] R. J. Warburton, H. Pillai, and R. C. Reineman, in *Proceedings of the IAG Symposium on Terrestrial Gravimetry: Static and Mobile Measurements (TG-SMM2010)*, 2010, Saint Petersburg, Russia, (2010).
[5] M. Campillo and A. Paul, Long-range correlations in the diffuse seismic coda, Science **299**, 547 (2003).
[6] N. M. Shapiro, M. Campillo, L. Stehly, and M. H. Ritzwoller, High-resolution surface-wave tomography from ambient seismic noise, Science **307**, 1615 (2005).
[7] R. Courtland, Earth science: Harnessing the Hum, Nature **453**, 146 (2008).
[8] M. V. Camp, H. G. Wenzel, P. Schott, P. Vauterin, and O. Francis, Accurate transfer function determination for superconducting gravimeters, Geophys. Res. Lett. **27**, 37 (2000).
[9] B. R. Arora, G. Rawat, N. Kumar, and V. M. Choubey, Multi-Parameter Geophysical Observatory: gateway to integrated earthquake precursory research, Curr. Sci. **103**, 1286 (2012).
[10] H.-F. Yang, Recent advances in imaging crustal fault zones: a review, Earthq. Sci. **28**, 151 (2015).
[11] C. Donaldson, C. Caudron, R. G. Green, W. A. Thelen, and R. S. White, Relative seismic velocity variations correlate with deformation at kīlauea volcano, Sci. Adv. **3**, 1 (2017).
[12] A. Mordret, T. D. Mikesell, C. Harig, B. P. Lipovsky, and G. A. Prieto, Monitoring southwest greenland's ice sheet melt with ambient seismic noise, Sci. Adv. **2**, e1501538 (2016).
[13] H. A. Chan and H. J. Paik, Superconducting gravity gradiometer for sensitive gravity measurements. I. Theory, Phys. Rev. D **35**, 3551 (1987).
[14] H. A. Chan, M. V. Moody, and H. J. Paik, Superconducting gravity gradiometer for sensitive gravity measurements. II. Experiment, Phys. Rev. D **35**, 3572 (1987).
[15] M. V. Moody, H. J. Paik, and E. R. Canavan, Three-axis superconducting gravity gradiometer for sensitive gravity experiments, Rev. Sci. Instrum. **73**, 3957 (2002).
[16] W. Vodel, S. Nietzsche, H. Koch, and G. J. V. Zameck, DC SQUID-based position detector for gravitational experiments, Appl. Supercond. **6**, 767 (1999).
[17] R. Scharnweber and J. M. Lumley, Characterization of a dc squid based accelerometer circuit for a superconducting gravity gradiometer, Supercond. Sci. Tech. **12**, 813 (1999).
[18] J. M. Lumly, J. P. White, G. Barnes, D. Huang, and H. J. Paik, in *Proceedings of the ASEG-PESA Airborne Gravity 2004 Workshop*, Sydney, Australia, 2004 (2004).
[19] X.-K. Liu, D. Ma, L. Chen, and X.-D. Liu, Tuning the stiffness balance using characteristic frequencies as a criterion

for a superconducting gravity gradiometer, Sensors **18**, 1 (2018).
[20] R. Torii, SQUID position sensor development, Class. Quantum Grav. **13**, 11A (1996).
[21] X.-D Liu and J. Luo, Chinese Patent No. 201810468722.8 (2018).
[22] H. B. Callen and T. A. Welton, Irreversibility and generalized noise, Phys. Rev. **83**, 34 (1951).
[23] H. B. Callen and R. F. Greene, On a theorem of irreversible thermodynamics, Phys. Rev. **86**, 702 (1952).
[24] P. R. Saulson, Thermal noise in mechanical experiments, Phys. Rev. D **42**, 2437 (1990).
[25] H. Nyquist, Thermal agitation of electric charge in conductors, Phys. Rev. **32**, 110 (1928).
[26] R. L. Fagaly, Superconducting quantum interference device instruments and applications, Rev. Sci. Instrum. **77**, 101101 (2006).